Journal of Materials Chemistry A

ROYAL SOCIETY OF CHEMISTRY

PAPER

View Article Online
View Journal | View Issue



Cite this: J. Mater. Chem. A, 2023, 11, 19083

# Exfoliated $NbSe_2$ nanosheet@polypyrrole hybrid nanocomposites as a high performance anode of lithium-ion batteries†

Byung-Ho Kang,‡[a] Seulgi Shin,‡[b] Kunwoo Nam,[a] Joonwon Bae,[c] Jong-Min Oh,[b] Sang-Mo Koo,[b] Hiesang Sohn,[d] Sung-Hoon Park *[a] and Weon Ho Shin *[b]

Received 4th March 2023
Accepted 15th August 2023

DOI: 10.1039/d3ta01335a

rsc.li/materials-a



Transition metal dichalcogenides (TMDCs), as next-generation two-dimensional materials, have gained considerable attention in energy storage applications through the incorporation of functional materials. In this work, we investigated $NbSe_2$ TMDCs possessing metallic properties through the exfoliation of mono/few layered nanosheets and their subsequent incorporation with polypyrrole, a conducting polymer. The charge–charge interaction between the positively charged pyrrole and negatively charged $NbSe_2$ nanosheets was facilitated through a chemical incorporation method, resulting in $NbSe_2$@polypyrrole hybrid nanocomposites where the pyrrole molecules polymerized along the surface of $NbSe_2$ nanosheets. The synergistic effect observed in $NbSe_2$@polypyrrole hybrid nanocomposites demonstrated high capacity for lithium storage (955 mA h $g^{-1}$) with excellent cycling stability (>100 cycles) and rate performance (4 A $g^{-1}$), surpassing the performance of pristine $NbSe_2$ or polypyrrole electrodes. In particular, the $NbSe_2$@polypyrrole hybrid nanocomposite exhibited 361 mA h $g^{-1}$ discharge capacity retention within a charge/discharge time of less than 6 minutes, which is comparable with the capacity of conventional graphite anodes. Our hybrid approach utilizing TMDCs and carbon structures could provide significant insight for the utilization of novel TMDC materials in energy storage applications.

## Introduction

Transition metal dichalcogenides (TMDCs) are next-generation 2-dimensional materials that have garnered attention due to their potential applications in various fields, including energy storage, conversion,[1–6] solar cells,[7,8] and electrocatalysis.[9–12] The layered structure of TMDC materials consists of strong covalent bonds along the *a* and *b* axes and weak non-covalent van der Waals interactions along the *c*-axis. TMDC materials follow an $MX_2$ stoichiometry, where M is a transition metal and X is a chalcogenide. This combination gives rise to unique electrical properties such as superconductivity, semi-conductivity, and insulation. $MoS_2$ is the most well-known TMDC composition in terms of its semiconducting properties, but researchers have been investigating other TMDC materials for their unique properties in electronic and energy devices.

Among various TMDCs, $NbSe_2$ has been gaining attention due to its metallic properties, although limited research has been conducted compared to that on $MoSe_2$ and $WSe_2$. Despite its potential as a superconducting material, $NbSe_2$ has not been thoroughly studied. Wang *et al.* synthesized monolayer $NbSe_2$ *via* chemical vapor deposition (CVD) and demonstrated its superconducting properties according to the number of layers and temperature.[13] Additionally, charge density waves and superconducting phases were observed in $NbSe_2$ down to a thickness of one monolayer, with the transition temperature increasing from 33 K in the bulk to 145 K in the monolayer by Xi *et al.*[14] Moreover, $NbSe_2$-based composite materials have also been studied for energy storage devices, both theoretically and experimentally. For example, Khan *et al.* reported visible light active photocatalytic $NbSe_2$@$TiO_2$ nanocomposites using the increased surface area and visible light absorption capability of $NbSe_2$.[10] Furthermore, Nguyen *et al.* synthesized $NbSe_2$@-graphene composites *via* wet ball milling as an anode material for lithium-ion batteries (LIBs).[4] $NbSe_2$ nanosheets embedded in carbon nanofibers co-doped with N and Se were used in a potassium-ion hybrid capacitor by Chen *et al.*[15] and Liu *et al.* reported a $WS_2$/$NbSe_2$ van der Waals heterostructure as an ultrafast charging and discharging anode material for LIBs.[16] Despite these efforts, there is still a need to develop $NbSe_2$-

[a]Department of Mechanical Engineering, Soongsil University, 369 Sangdo-ro, Dongjakgu, Seoul 06978, Republic of Korea. E-mail: leopark@ssu.ac.kr
[b]Department of Electronic Materials Engineering, Kwangwoon University, Seoul 01897, Republic of Korea. E-mail: weonho@kw.ac.kr
[c]Department of Applied Chemistry, Dongduk Women's University, Seoul 02748, Republic of Korea
[d]Department of Chemical Engineering, Kwangwoon University, Seoul 01897, Republic of Korea

† Electronic supplementary information (ESI) available. See DOI: https://doi.org/10.1039/d3ta01335a

‡ These authors contributed equally to this work.

based materials with controlled properties for next-generation energy and electronic applications.

Utilization of TMDC materials often requires a monolayer of the material. Chemical vapor deposition (CVD) is typically used to prepare monolayer TMDCs due to its potential to synthesize high-quality and large-sized TMDC layers.[13,17] However, the high cost of the high vacuum system and the limited amount of synthetic materials hinder versatile applications. An alternative method for large-scale synthesis of monolayer TMDCs is the Li intercalation/exfoliation process, where Li atoms intercalate into weak van der Waals interlayers.[18–20] In this work, we successfully synthesized monolayer $NbSe_2$ through the Li intercalation/exfoliation process. The prepared $NbSe_2$ nanosheets were combined with a conducting polymer to enhance their electrical transport properties. Polypyrrole (PPy) is a promising conducting polymer with a nitrogen-containing conjugated structure that can provide higher electronic conductivity than carbon alone.[21–23]

Numerous studies have reported PPy's cost-effectiveness, environmental stability, and simple fabrication.[3,24–26] Moreover, PPy is a positively charged conducting polymer that can readily realize a composite structure with negatively charged $NbSe_2$ monolayer nanosheets. Therefore, we fabricated an $NbSe_2$@PPy hybrid nanocomposite structure as an anode material for a lithium-ion battery for the first time. The prepared $NbSe_2$@PPy structures exhibited (i) a high gravimetric capacity of 955 mA h $g^{-1}$, (ii) stable operation for more than 300 cycles without any capacity loss, and (iii) comparable capacity (361 mA h $g^{-1}$) with conventional graphite anodes within 6 min of discharge time. Overall, the hybrid TMDC structure with $NbSe_2$ and the PPy composite showed outstanding power and cycling performance that could be used to realize sustainable energy storage systems.

## Experimental section

### Materials for $NbSe_2$@PPy synthesis

Bulk niobium diselenide powders ($NbSe_2$, >99.8%) were purchased from Alfa Aesar. 1.6 M *n*-butyllithium solution, iron(III) chloride hexahydrate (>97.0%), polyvinylidene fluoride (PVdF), *N*-methyl-2-pyrrolidinone (NMP, >99%), hexane (>97.0%), and ethanol were obtained from Sigma Aldrich. A pyrrole monomer was purchased from Tokyo Chemical Industry. Cu foil as a current collector and Li foil used were purchased from Wellcos Corp. The liquid electrolyte was prepared by using 1 M $LiPF_6$ solution of ethylene carbonate (EC) and ethyl methyl carbonate (EMC) (EC : EMC = 3 : 7 v/v) in the same volume and purchased from Soulbrain Co. CR2032 coin cells for electrochemical testing were purchased from Wellcos Corp.

### Exfoliation of $NbSe_2$ nanosheets

The $NbSe_2$ powders were placed into a vial and in order to achieve inert conditions nitrogen gas was purged. Then, *n*-butyllithium solution (10 mL) was injected into the vial. After this, the solution was sonicated in a sonication bath at 60 °C, 375 W for 90 min. While lithium-ions intercalated into the layers, some unreacted ions remained. Thus, the washing process was performed two times using hexane. Then, deionized water was injected into the lithium intercalated $NbSe_2$ powders to activate the reaction between lithium-ions and water. During the reaction, hydrogen gas, which is the main driving force to exfoliate the layers was generated. Finally, the $NbSe_2$ suspension was centrifuged to select mono- or few-layer $NbSe_2$ nanosheets at 600 rpm for 20 min (Fig. 1a). The sediments obtained after centrifugation could be redispersed through additional sonication for 5 min to increase the amount of nanosheets.

### Synthesis of $NbSe_2$@PPy hybrid nanocomposites

The $NbSe_2$@PPy hybrid nanocomposites were fabricated according to the following procedure. First, the concentration of the exfoliated $NbSe_2$ dispersion was calculated through the Beer–Lambert law. Then, different volumes of $NbSe_2$ dispersion were prepared to synthesize composites with different weight ratios of $NbSe_2$ to PPy. Hence, two types of $NbSe_2$@PPy composites could be synthesized (named $NbSe_2$@PPy-1 and $NbSe_2$@PPy-2, respectively). The pyrrole monomer (1 g) was dropped into the as-prepared $NbSe_2$ dispersion and stirred for 1 hour at 500 rpm. This step was for promoting sufficient charge–charge interaction between the negative charge of $NbSe_2$ nanosheets and positive charge of the pyrrole monomer. After this, *in situ* polymerization was initiated by adding $FeCl_3$ aqueous solution and stirred under the same conditions (the weight ratio of $FeCl_3$ to pyrrole was 2.3 : 1). Finally, the $NbSe_2$@PPy hybrid nanocomposite solution was filtered through a paper filter. Obtained powders were washed using ethanol (twice a day for 2 days) and di-water (twice a day for a day) to remove unwanted residues. Then, the prepared powders were dried in an oven at 70 °C for 6 hours. The carbonization is performed at 800 °C under an Ar atmosphere.

### Materials characterization

Scanning electron microscopy (SEM) and an energy dispersive spectrometer (EDS) were used to measure the morphologies of nanomaterials. Atomic force microscopy (AFM) was performed to confirm the thickness of the $NbSe_2$ nanosheet. Raman spectra were obtained by introducing a Raman spectrometer (Horiba Jobin Yvon) which operated at a laser wavelength of 532 nm. The concentration of the $NbSe_2$ suspension was measured using an ultraviolet-visible (UV-vis) spectrometer. The actual weight ratio of $NbSe_2$ to PPy was calculated through thermogravimetric analysis (TGA), heated from 25 °C to 900 °C with a 10 °C $min^{-1}$ heating rate under an air atmosphere. X-ray photoelectron spectroscopy (XPS) was performed for analyzing the chemical structure of the as-synthesized materials.

### Electrochemical measurement

The synthesized $NbSe_2$@PPy, PPy, and $NbSe_2$ were used as active materials for an LIB anode. The samples were prepared as a paste with *N*-methyl-2-pyrrolidone (NMP) by mixing activated carbon as a conduction agent and polyvinylidene fluoride

 

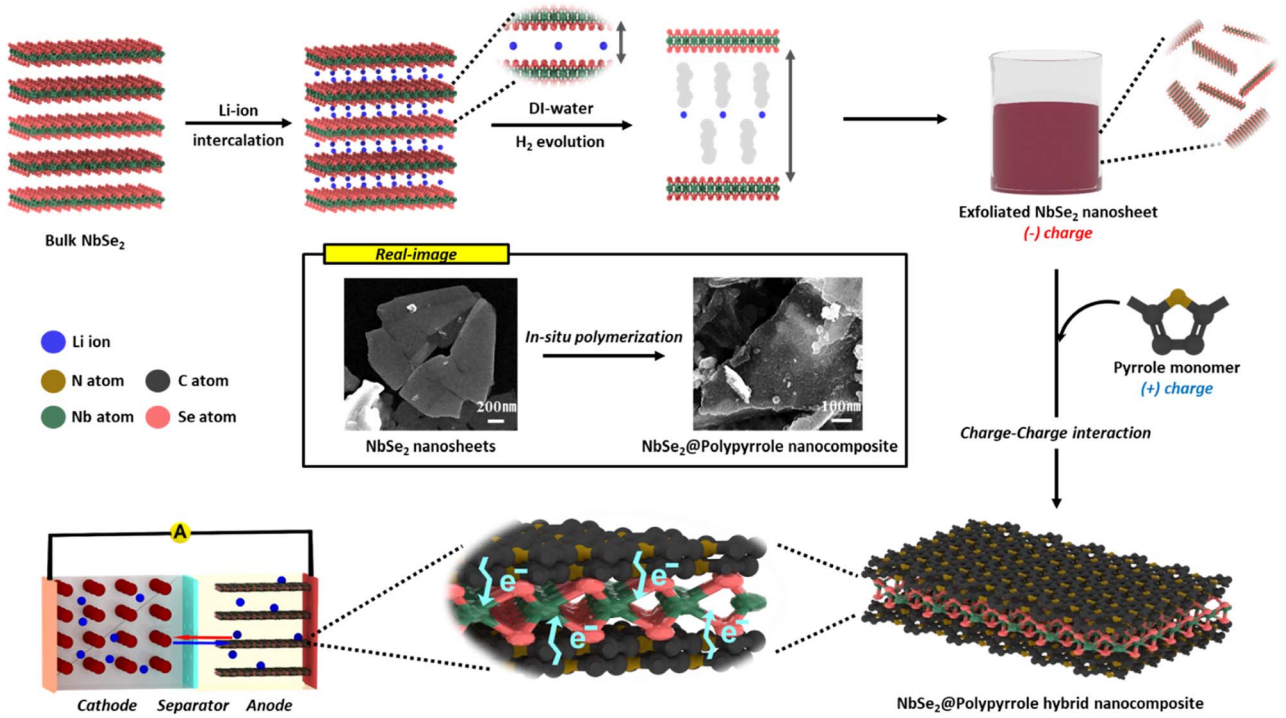


Fig. 1 Schematic illustrations of $NbSe_2$@PPy hybrid nanocomposite preparation; lithium-ion intercalation process and *in situ* polymerization *via* charge–charge interaction. Inset images show the SEM images of exfoliated $NbSe_2$ nanosheets and $NbSe_2$@PPy nanocomposites.

(PVdF) as a binder in a weight ratio of 8 : 1:1, and cast on Cu foil as a current collector. The mass loading of each electrode was about 1.0 mg $cm^{-2}$. The coin-type cells were assembled using Li foil as a counter electrode and a polyethylene separator. The 1 M $LiPF_6$ solution of ethylene carbonate (EC) and ethyl methyl carbonate (EMC) (EC : EMC = 3 : 7 v/v) electrolyte was used for the whole electrochemical test. Cyclic voltammetry (CV), galvanostatic charge–discharge (GCD), and cycle tests were conducted in a voltage range of 0.01–3 V. Cell tests were performed on a battery testing machine (Won-A Tech, WBCS3000Ls32). Electrochemical impedance spectroscopy (EIS) was performed using an open circuit in a frequency range of 1 MHz–0.01 Hz and at an amplitude of 5 mV. The EIS measurements were performed on a single-channel electrochemical workstation (Won-A Tech, WEISS500).

## Results and discussion

Fig. 1 describes a schematic illustration of the whole process from $NbSe_2$ exfoliation to PPy composite preparation. The intercalation originated from the strong reducing agent butyllithium, where the small sized Li ions intercalate between the van der Waals interlayers with the reduction reaction of the mother matrix layers. As a result, Li ions expand the interlayer space and weaken the van der Waals forces. Furthermore, the intercalated Li atoms explosively react with water by the following chemical reaction (1).

$$2Li + 2H_2O \rightarrow H_2\ (gas) + 2LiOH\ (aq.) \quad (1)$$

The resultant $H_2$ gas is the driving force of $NbSe_2$ exfoliation. During the intercalation reaction, the $NbSe_2$ layers reduce to have a partially negative charge, and exfoliated $NbSe_2$ nanosheets are also charged negatively to stably disperse in polar solvent (water). The reddish solution (shown in Fig. 1) is obtained after centrifugation, confirming that $NbSe_2$ is successfully exfoliated by the Li intercalation process. After exfoliation, we coated PPy on both sides of $NbSe_2$ monolayer nanosheets, with the charge–charge interaction between negatively charged $NbSe_2$ nanosheets[27,28] and the positively charged pyrrole monomer.[3] Due to the tendency of the resultant suspension of Li ion intercalation to restack, it is preferred to synthesize with PPy immediately after exfoliation. The high binding between $NbSe_2$ and PPy originated from coulombic forces and the precipitates could be obtained after pyrrole polymerization. The conducting polymer facilitates the electronic transport to the $NbSe_2$ nanosheet which could lead to the promotion of the electrochemical reactions.

The morphology of the $NbSe_2$ nanosheets after exfoliation is depicted in Fig. 2. As shown in Fig. 2a, bulk $NbSe_2$ powders are composed of a layered structure held together by weak van der Waals interactions, making it easy for foreign species to intercalate between the layers. In this work, we used butyllithium for Li intercalation with the reduction of $NbSe_2$ layers. The SEM image of exfoliated $NbSe_2$ monolayer nanosheets after spin coating on a Si wafer is presented in Fig. 2b. The large lateral sizes of $NbSe_2$ nanosheets range from 200 nm to 5 μm, with no significant size reduction. The UV-vis spectrum of exfoliated

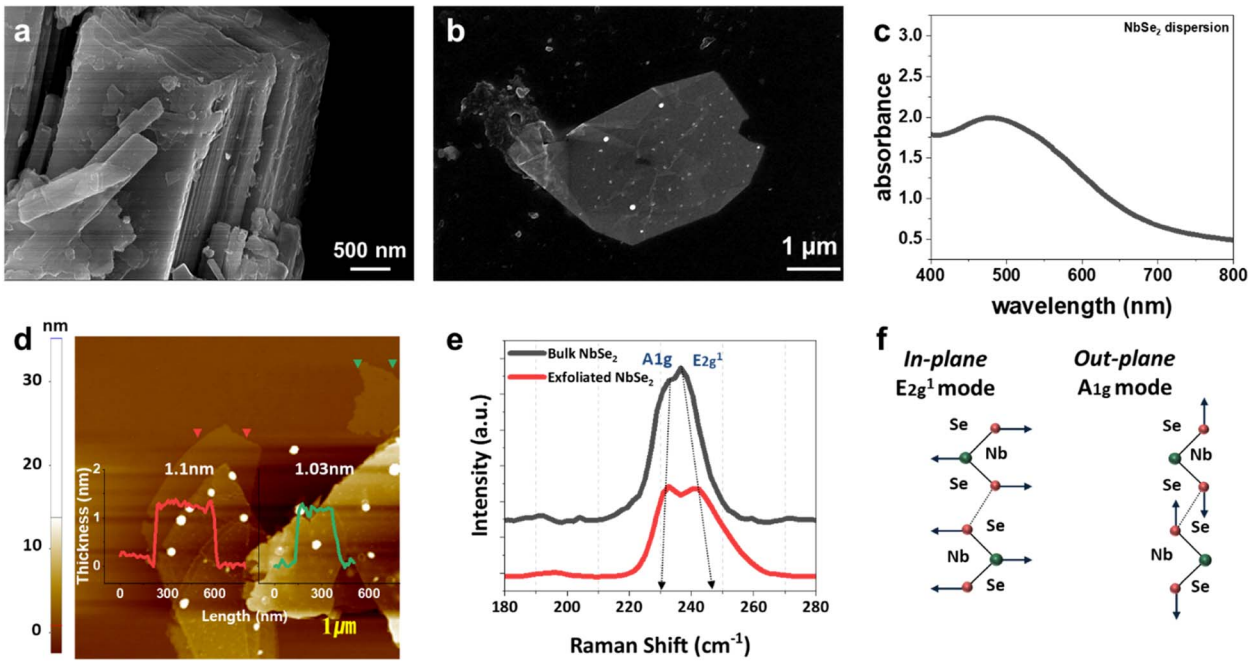


Fig. 2 (a) SEM images of bulk type $NbSe_2$ and (b) exfoliated $NbSe_2$ nanosheets, (c) UV-vis spectroscopy spectra of an exfoliated $NbSe_2$ nanosheet dispersion, (d) AFM images of exfoliated $NbSe_2$ nanosheets, (e) Raman spectroscopy spectra of bulk $NbSe_2$ and exfoliated $NbSe_2$ nanosheets, and (f) schematic images of major vibration modes of $NbSe_2$.

$NbSe_2$ solution is shown in Fig. 2c. Since $NbSe_2$ is metallic, a broad spectrum can be detected within the visible light range (Fig. 2c).[7,29–31] The AFM images in Fig. 2d show the thickness of exfoliated $NbSe_2$ nanosheets, and the apparent thickness of $NbSe_2$ nanosheets is ~1 nm.[32,33] This implies that the exfoliated $NbSe_2$ nanosheets mostly consist of monolayers. Raman analysis was performed to compare the chemical bonding nature of bulk and exfoliated $NbSe_2$ (shown in Fig. 2e). Bulk $NbSe_2$ displays main characteristic peaks of ~240 $cm^{-1}$ and ~230 $cm^{-1}$, representing the in-plane vibration mode and out-of-plane vibration mode, respectively, denoted as $E^1_{2g}$ and $A_{1g}$. The mechanism of in-plane and out-of-plane vibration modes is displayed in Fig. 2f. After exfoliation, two major features are observed. The peak of $E^1_{2g}$ vibration mode in exfoliated $NbSe_2$ nanosheets red-shifts compared to that in bulk $NbSe_2$ powder (from 236.57 $cm^{-1}$ to 242.30 $cm^{-1}$), while the $A_{1g}$ vibration mode is blue-shifted (from 232.74 $cm^{-1}$ to 230.83 $cm^{-1}$). This is consistent with previous reports.[14,34,35] Since these characterization peaks depend on the number of layers, the interlayer interaction between the layers is weakened, and the intralayer interaction within the layers becomes stronger for properly exfoliated $NbSe_2$ nanosheets. In summary, we successfully fabricated $NbSe_2$ nanosheets through the Li intercalation and exfoliation process.

The morphology of the $NbSe_2$@PPy composite is presented in Fig. 3, displaying its 2D sheet structure, similar to that of $NbSe_2$ alone (as depicted in Fig. 2b), while PPy has a sphere-shaped structure (see Fig. S1a and b†). It is well-known that randomly distributed PPy in a solvent tends to form spherical structures to reduce surface energy. When $NbSe_2$ nanosheets are introduced during the polymerization of pyrrole monomers, PPy deposits on the $NbSe_2$ nanosheets and follows their morphology. The coulombic interaction between positively charged pyrrole and negatively charged $NbSe_2$ nanosheets leads to strong binding between them. Therefore, the adsorbed pyrrole monomers on $NbSe_2$ nanosheets are polymerized when an initiator is introduced. The EDS mapping images presented in Fig. S1c and d† clearly show the homogeneous carbon structure coated on $NbSe_2$ nanosheets without any agglomeration. Moreover, we have prepared another composition with a lower amount of PPy, and there is no detectable difference in morphology, as shown in Fig. 3. Hereafter, we refer to the

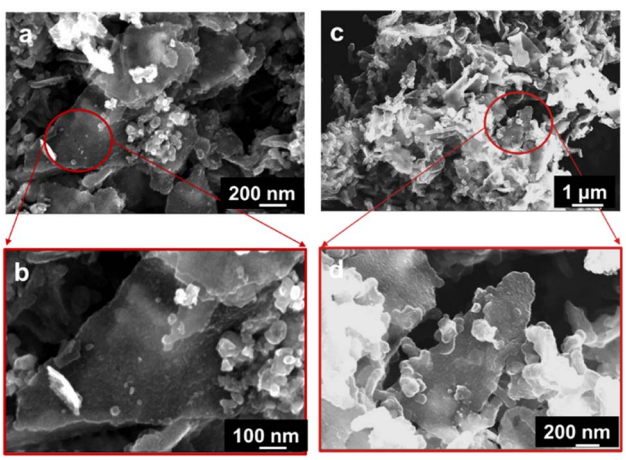


Fig. 3 SEM images of (a and b) $NbSe_2$@PPy-1 and (c and d) $NbSe_2$-PPy-2.

samples with a high amount of PPy and a low amount of PPy as $NbSe_2$@PPy-1 and $NbSe_2$@PPy-2, respectively.

The TGA analysis is performed to estimate the ratio of $NbSe_2$ and PPy in $NbSe_2$@PPy composites as shown in Fig. 4a. Pristine $NbSe_2$ stays without any noticeable change up to 900 °C, while the $NbSe_2$@PPy composites show a significant mass drop near 400 °C, which originated from the dissociation of PPy.[36] Therefore, the mass ratio of $NbSe_2$ in $NbSe_2$@PPy composites is calculated at 28% for $NbSe_2$@PPy-1 and 64% for $NbSe_2$@PPy-2. The Raman spectra of $NbSe_2$@PPy composites are presented in Fig. 4b to investigate the crystallinity of the carbon structure (PPy). Two distinguishable peaks are detected: the D-band (1344 $cm^{-1}$), attributed to defects or disorder of the carbon structure and the G-band (1570 $cm^{-1}$), commonly attributed to the graphite carbon structure.[37,38] The crystallinity of carbon-based materials can be compared by calculating the intensity ratio of the D-band and G-band. The $I_D/I_G$ ratios of all samples in this study are comparable ($I_D/I_G = \sim 0.89$), indicating that the coated carbon structure does not significantly change with the introduction of $NbSe_2$ nanosheets during the polymerization process. Therefore, we can directly compare the effect of $NbSe_2$ nanosheets on the following lithium storage properties.

The XPS spectra are shown in Fig. 4c–f to determine the electronic states of the elements and composition of $NbSe_2$@PPy composites. From the survey scan in Fig. 4c, the Nb 3d and Se 3d peaks are easily detected on the $NbSe_2$@PPy hybrid. The N 1s detailed spectrum in Fig. 4d has two different peaks. The higher binding energy peak (400.6 eV) represents the quaternary nitrogen where the nitrogen atoms replace the carbon structure, and the lower binding energy peak (398 eV) is attributed to the pyridinic nitrogen. The nitrogen configuration is a typical feature of annealed PPy as reported elsewhere.[39] A similar N 1s spectrum is found for PPy and the $NbSe_2$@PPy hybrid, indicating that the presence of $NbSe_2$ nanosheets does not alter the PPy structure. The detailed spectra of Nb and Se for $NbSe_2$@PPy are shown in Fig. 4e and f. The $3d_{2/3}$ (209 eV) and $3d_{2/5}$ (206.2 eV) peaks for Nb 3d and $3d_{2/3}$ (56.2 eV) and $3d_{2/5}$ (55.4 eV) peaks for Se 3d are detected, consistent with other reports.[7,40] This indicates that the chemical structure of $NbSe_2$ nanosheets is maintained during synthesis of $NbSe_2$@PPy. Therefore, we can conclude that the $NbSe_2$@PPy hybrid nanocomposites are successfully synthesized.

The prepared $NbSe_2$@PPy materials were utilized as LIB anode materials, and their electrochemical properties were compared to those of $NbSe_2$ and PPy alone. Fig. 5a displays the CV graphs of the $NbSe_2$@PPy sample obtained at a 0.5 mV $s^{-1}$ scan rate for the first four cycles, illustrating redox reactions during the lithiation/delithiation process. The low potential peaks observed below 1 V originate from the formation of a solid–electrolyte interface (SEI) layer on the active materials through the decomposition of the liquid electrolyte.[4] In the second cycle, distinct oxidation/reduction peaks were observed at ~1.4 V for the cathodic peak and ~1.7 V for the anodic peak. This phenomenon can be attributed to the lithiation/delithiation of $NbSe_2$ nanosheets, which follows the electrochemical reaction mechanism (2).

$$NbSe_2 + 4Li^+ + 4e^- \leftrightarrow 2Li_2Se + Nb \quad (2)$$

The theoretical capacity of $NbSe_2$ conversion based on the above reaction is approximately 1538 mA h $g^{-1}$. According to other literature studies, the lithiation process in the $NbSe_2$ system starts with the intercalation of $Li^+$ between the $NbSe_2$ layers before the above-mentioned conversion mechanism occurs.[41] To investigate this process, we performed cyclic voltammetry (CV) measurements on the pristine $NbSe_2$ electrode, as shown in Fig. S2.† The results displayed the intercalation peak at approximately 2 V. However, the $NbSe_2$@PPy composite electrodes (Fig. 5a) are composed of mono- or few-layers of

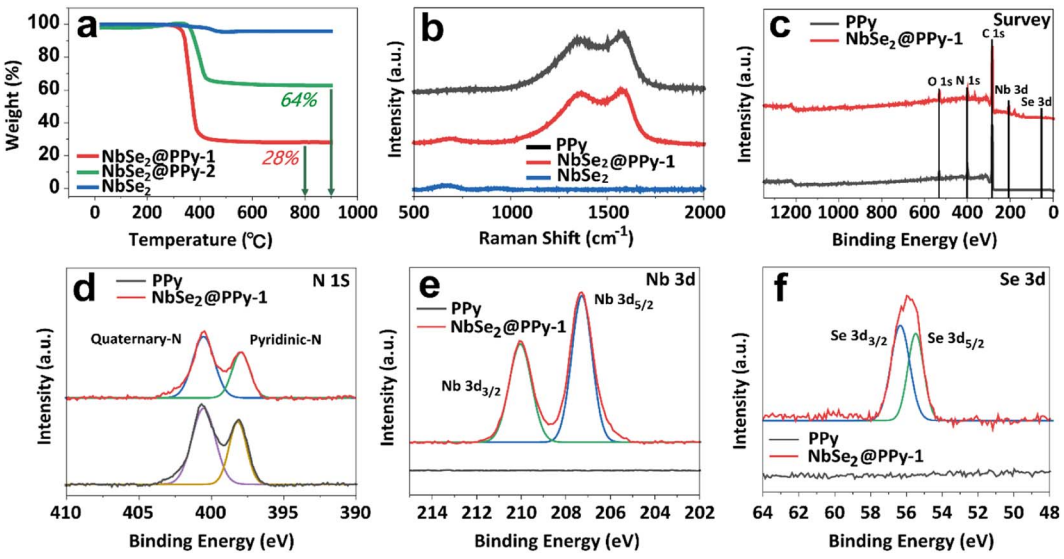


Fig. 4 (a) TGA curves of $NbSe_2$, $NbSe_2$@PPy-1, and $NbSe_2$@PPy-2. (b) Raman spectra of PPy, $NbSe_2$@PPy, and $NbSe_2$. (c) XPS survey scan, (d) N 1s detailed scan, (e) Nb 3d detailed scan, and (f) Se 3d detailed scan of PPy and $NbSe_2$@PPy.

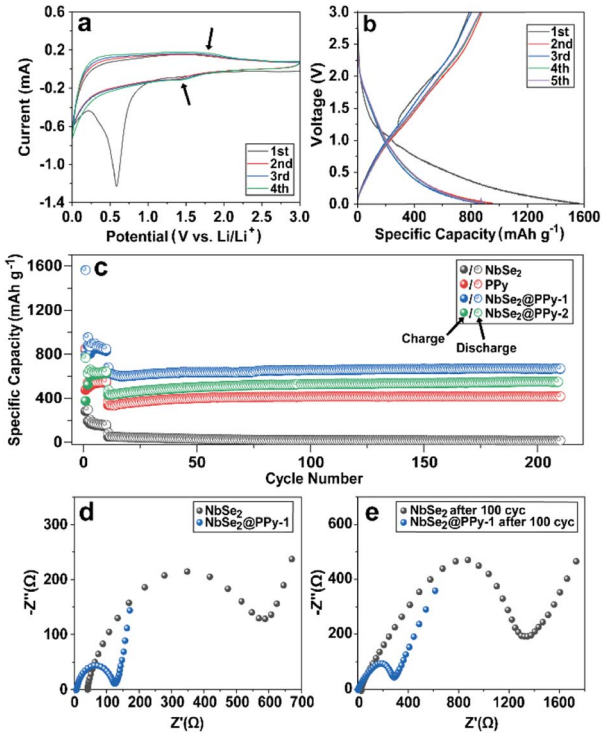


Fig. 5 (a) CV graphs of $NbSe_2$@PPy-1 for the first 4 cycles, (b) GCD graphs of $NbSe_2$@PPy-1 for the first 5 cycles, (c) cyclic retention of $NbSe_2$@PPy-1, $NbSe_2$@PPy-2, $NbSe_2$, and PPy. (d) Nyquist plots of $NbSe_2$ and $NbSe_2$-PPy-1 before cycling, and (e) Nyquist plots of $NbSe_2$ and $NbSe_2$-PPy-1 after 100 cycles.

$NbSe_2$, and therefore, the $Li^+$ intercalation process hardly occurs. After one cycle, the CV graphs were almost identical to those in the second cycle, indicating excellent stability and reversibility of the $NbSe_2$@PPy electrode system. In contrast, the CV graph of the PPy electrode did not exhibit noticeable peaks, which is typical of amorphous carbon structures. Only the peaks of SEI formation (below 1 V) were detected in the first cycle.

Fig. 5b presents the galvanostatic charge–discharge (GCD) profiles of the $NbSe_2$@PPy-1 electrode system at a current density of 0.1 A $g^{-1}$ for the first five cycles. The $NbSe_2$@PPy-1 electrode system displays a high capacity of approximately 1562 mA h $g^{-1}$ with a coulombic efficiency of 50.5% during the first discharge. The major electrochemical reaction in $NbSe_2$@PPy-1 occurs from around 1.5 V due to the electrochemical conversion reaction of $NbSe_2$ nanosheets in PPy. The potential of $NbSe_2$@PPy-1 decreases without a distinct plateau, indicating that the solid solution reaction occurs on the active materials during the lithiation/delithiation process. The low coulombic efficiency during the first cycle is due to the formation of the solid–electrolyte interface (SEI) layer, which is consistent with the aforementioned cyclic voltammetry (CV) results. From the second cycle, the discharge capacity remains stable at approximately 955 mA h $g^{-1}$ with a high coulombic efficiency of 92%. In contrast, the $NbSe_2$ electrode alone has a first discharge capacity of only 837 mA h $g^{-1}$ at a current density of 0.1 A $g^{-1}$ (Fig. S3†), which is less than the theoretical capacity of the reaction (1). The discharge capacity of the $NbSe_2$ electrode gradually decreases to 175 mA h $g^{-1}$ after five cycles at a current density of 0.1 A $g^{-1}$, which is attributed to the low intrinsic electrical conductivity of $NbSe_2$. $NbSe_2$ with a stacked structure has low electrochemical activity, which may be present near the surface. In contrast, the well-coated $NbSe_2$@PPy-1 structure exhibits great reversibility because the highly conductive PPy readily transfers electrons from the current collector to the active $NbSe_2$, and the porous structure of PPy could deliver $Li^+$ ions to $NbSe_2$.

Fig. 5c displays the cycling performances of $NbSe_2$, PPy, $NbSe_2$@PPy-1, and $NbSe_2$@PPy-2 at a current density of 0.5 A $g^{-1}$. The first five cycles are performed at a current density of 0.1 A $g^{-1}$ for the stabilization of the electrodes. The discharge capacity of the $NbSe_2$@PPy-1 electrode in the 210th cycle reaches approximately 670 mA h $g^{-1}$, while the $NbSe_2$ electrode is significantly degraded to 17 mA h $g^{-1}$ in the 210th cycle. The coulombic efficiency of every cycle is around 99% for the $NbSe_2$@PPy-1 electrode, indicating highly reversible electrochemical reactions. The PPy and $NbSe_2$@PPy-2 electrodes have discharge capacities of 416 mA h $g^{-1}$ and 531 mA h $g^{-1}$, respectively, in the 100th cycle, with high cycling stability. Notably, the $NbSe_2$@PPy-2 electrode has a higher $NbSe_2$ content than the $NbSe_2$@PPy-1 electrode. Since the PPy on the $NbSe_2$@PPy-2 electrode is not homogeneously covered on the $NbSe_2$ nanosheets, the $NbSe_2$@PPy-2 electrode may have lower electrochemical activity.

In order to investigate the electrochemical mechanism of the $NbSe_2$@PPy-1 electrode, we conducted EIS measurements. As shown in Fig. 5d, the semicircle in the high frequency region corresponds to the charge transfer resistance ($R_{ct}$), while the straight line in the low frequency region corresponds to the Warburg impedance related to the mass transfer. The $R_{ct}$ value of $NbSe_2$@PPy-1 for the as-prepared cell is 126 Ω, which is significantly lower than that of the $NbSe_2$ electrode (589 Ω). This improvement in $R_{ct}$ is attributed to the enhanced electron mobility resulting from the well-coated PPy on the $NbSe_2$@PPy-1 electrode. Furthermore, after 100 cycles of lithiation/delithiation, the $R_{ct}$ value of $NbSe_2$@PPy-1 is 287 Ω (Fig. 5e), which is 128% higher than that in the first cycle, while the $R_{ct}$ of the $NbSe_2$ electrode increases significantly (1322 Ω). These results indicate that our $NbSe_2$@PPy-1 electrode exhibits significant improvements in capacity and stability simultaneously.

The rate performances of the $NbSe_2$, PPy, $NbSe_2$@PPy-1, and $NbSe_2$@PPy-2 electrodes were evaluated by varying the current density from 0.1 A $g^{-1}$ to 4 A $g^{-1}$, as shown in Fig. 6a. The PPy, $NbSe_2$@PPy-1, and $NbSe_2$@PPy-2 electrodes exhibit reversible lithiation/delithiation reactions even at high rates of 4 A $g^{-1}$, while the $NbSe_2$ electrode degrades after a few cycles. The discharge capacity of the $NbSe_2$@PPy-1 electrode is 361 mA h $g^{-1}$ at a current density of 4 A $g^{-1}$, which is 58.9% lower than that at 0.1 A $g^{-1}$. The discharge capacities of the PPy and $NbSe_2$@PPy-2 electrodes are 178 mA h $g^{-1}$ and 286 mA h $g^{-1}$, respectively, at a current density of 4 A $g^{-1}$. After 5 cycles at 4 A $g^{-1}$, the current density was changed back to the initial state of 0.1 A $g^{-1}$, and the discharge capacity of the $NbSe_2$@PPy-1

 

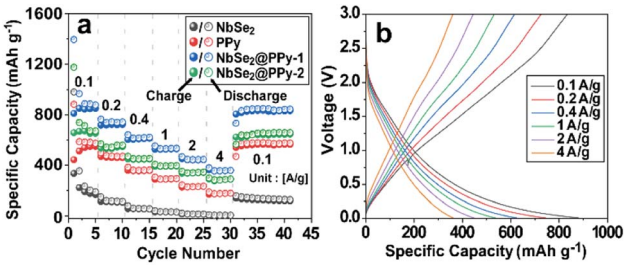


Fig. 6 (a) Rate performance of $NbSe_2$@PPy-1, $NbSe_2$@PPy-2, $NbSe_2$, and PPy, (b) GDC graphs of $NbSe_2$@PPy-1 by increasing the current density from 0.1 A $g^{-1}$ to 4 A $g^{-1}$.

electrode returned to the initial value of 819 mA h $g^{-1}$, indicating excellent electrochemical stability at high current densities. In contrast, the $NbSe_2$ nanosheet electrode exhibits significant degradation at high current densities and poor rate performance. The GCD profiles of $NbSe_2$@PPy-1, $NbSe_2$, PPy, and $NbSe_2$@PPy-2 electrodes for different current densities from 0.1 A $g^{-1}$ to 4 A $g^{-1}$ are displayed in Fig. 6b and S5a–c.† Therefore, the $NbSe_2$@PPy hybrid nanocomposites show high performance anode properties in terms of high capacity, fast kinetics, and excellent stability, which makes it possible to apply them to next generation energy storage devices.

## Conclusions

We investigated the potential of chemically exfoliated TMDC-based nanocomposite materials as high-performance lithium-ion battery electrodes. We utilized Li-intercalation to exfoliate $NbSe_2$ and obtained mono/few layer $NbSe_2$ nanosheets. These nanosheets possess a negative charge that easily interacts with positively charged pyrrole molecules through charge–charge interactions. Pyrrole polymerization subsequently occurs on the exfoliated $NbSe_2$ nanosheets, with a negligible effect on their structure. The novel $NbSe_2$@PPy hybrid nanocomposites exhibit a synergetic effect of high electrical conductivity from coated PPy and high capacity from $NbSe_2$ nanosheets. While $Li^+$ ions intercalate irreversibly into the van der Waals gap between the $NbSe_2$ interlayer on pristine $NbSe_2$, the exfoliated $NbSe_2$@-PPy hybrid shows only a reversible conversion reaction. The $NbSe_2$@PPy nanocomposites exhibit an initial capacity of 1562 mA h $g^{-1}$, and consistently sustain a stable performance, maintaining 670 mA h $g^{-1}$ over 210 cycles at a current density of 0.5 A $g^{-1}$. Furthermore, the $NbSe_2$@PPy nanocomposites exhibit high-rate stability at 4 A $g^{-1}$ current density with 361 mA h $g^{-1}$ capacity, which is comparable with that of commercial graphite anodes. Our strategy of utilizing exfoliated TMDC@PPy hybrid nanocomposites has great potential for energy storage applications as high-capacity and stable anode materials in LIBs, considerably.

## Author contributions

Byung-Ho Kang: methodology, validation, writing – original draft. Seulgi Shin: Methodology, validation, writing – original draft. Kunwoo Nam: methodology. Joonwon Bae: methodology, validation. Jong-Min Oh: investigation and methodology. Sang-Mo Koo: methodology. Hiesang Sohn: investigation. Sung-Hoon Park: conceptualization, funding acquisition, supervision, writing, and editing. Weon Ho Shin: conceptualization, funding acquisition, writing, review, and editing.

## Conflicts of interest

The authors declare no conflicts of interest.

## Acknowledgements

This work was supported by a National Research Foundation of Korea (NRF) grant funded by the Korean government (MSIT) (No. 2020R1A2C1013489 and RS-2023-00222124). This work was also supported by a Korea Institute for Advancement of Technology (KIAT) grant funded by the Korea Government (MOTIE) (P0012451, The Competency Development Program for Industry Specialist).

## References

1 M. Chhowalla, H. S. Shin, G. Eda, L. J. Li, K. P. Loh and H. Zhang, *Nat. Chem.*, 2013, **5**, 263–275.
2 E. Hitz, J. Wan, A. Patel, Y. Xu, L. Meshi, J. Dai, Y. Chen, A. Lu, A. V. Davydov and L. Hu, *ACS Appl. Mater. Interfaces*, 2016, **8**, 11390–11395.
3 Y. K. Kim, H. Jeon, D. Han and K.-Y. Shin, *J. Alloys Compd.*, 2021, 868.
4 Q. H. Nguyen, H. Kim, I. T. Kim, W. Choi and J. Hur, *Chem. Eng. J.*, 2020, 382.
5 B. Xu, X. Ma, J. Tian, F. Zhao, Y. Liu, B. Wang, H. Yang and Y. Xia, *Ionics*, 2019, **25**, 4171–4177.
6 J. Xu, J. Zhang, W. Zhang and C.-S. Lee, *Adv. Energy Mater.*, 2017, **7**, 1700571.
7 X. Gu, W. Cui, T. Song, C. Liu, X. Shi, S. Wang and B. Sun, *ChemSusChem*, 2014, **7**, 416–420.
8 M. A. Ibrahem, W.-C. Huang, T.-w. Lan, K. M. Boopathi, Y.-C. Hsiao, C.-H. Chen, W. Budiawan, Y.-Y. Chen, C.-S. Chang, L.-J. Li, C.-H. Tsai and C. W. Chu, *J. Mater. Chem. A*, 2014, **2**, 11382–11390.
9 X. Chia, A. Ambrosi, P. Lazar, Z. Sofer and M. Pumera, *J. Mater. Chem. A*, 2016, **4**, 14241–14253.
10 R. Khan, A. Riaz, M. Rabeel, S. Javed, R. Jan and M. A. Akram, *Appl. Nanosci.*, 2019, **9**, 1915–1924.
11 J. Wang, X. Liu, Y. Liu and G. Yang, *Nanomaterials*, 2019, **9**, 751.
12 Y. Yu, G. H. Nam, Q. He, X. J. Wu, K. Zhang, Z. Yang, J. Chen, Q. Ma, M. Zhao, Z. Liu, F. R. Ran, X. Wang, H. Li, X. Huang, B. Li, Q. Xiong, Q. Zhang, Z. Liu, L. Gu, Y. Du, W. Huang and H. Zhang, *Nat. Chem.*, 2018, **10**, 638–643.
13 H. Wang, X. Huang, J. Lin, J. Cui, Y. Chen, C. Zhu, F. Liu, Q. Zeng, J. Zhou, P. Yu, X. Wang, H. He, S. H. Tsang, W. Gao, K. Suenaga, F. Ma, C. Yang, L. Lu, T. Yu, E. H. T. Teo, G. Liu and Z. Liu, *Nat. Commun.*, 2017, **8**, 394.

14 X. Xi, L. Zhao, Z. Wang, H. Berger, L. Forro, J. Shan and K. F. Mak, *Nat. Nanotechnol.*, 2015, **10**, 765–769.
15 M. Chen, L. Wang, X. Sheng, T. Wang, J. Zhou, S. Li, X. Shen, M. Zhang, Q. Zhang, X. Yu, J. Zhu and B. Lu, *Adv. Funct. Mater.*, 2020, **30**, 2004247.
16 H. Liu, Z. Huang, G. Wu, Y. Wu, G. Yuan, C. He, X. Qi and J. Zhong, *J. Mater. Chem. A*, 2018, **6**, 17040–17048.
17 Y. H. Lee, X. Q. Zhang, W. Zhang, M. T. Chang, C. T. Lin, K. D. Chang, Y. C. Yu, J. T. Wang, C. S. Chang, L. J. Li and T. W. Lin, *Adv. Mater.*, 2012, **24**, 2320–2325.
18 M. Rajapakse, B. Karki, U. O. Abu, S. Pishgar, M. R. K. Musa, S. M. S. Riyadh, M. Yu, G. Sumanasekera and J. B. Jasinski, *npj 2D Mater. Appl.*, 2021, 5.
19 Z. Zeng, Z. Yin, X. Huang, H. Li, Q. He, G. Lu, F. Boey and H. Zhang, *Angew Chem. Int. Ed. Engl.*, 2011, **50**, 11093–11097.
20 Q. Zhang, L. Mei, X. Cao, Y. Tang and Z. Zeng, *J. Mater. Chem. A*, 2020, **8**, 15417–15444.
21 Y. Deng, Y. Xie, K. Zou and X. Ji, *J. Mater. Chem. A*, 2016, **4**, 1144–1173.
22 H. M. Jeong, J. W. Lee, W. H. Shin, Y. J. Choi, H. J. Shin, J. K. Kang and J. W. Choi, *Nano Lett.*, 2011, **11**, 2472–2477.
23 J. H. Lim, J. H. Won, M. K. Kim, D. S. Jung, M. Kim, C. Park, S.-M. Koo, J.-M. Oh, H. M. Jeong, H. Sohn and W. H. Shin, *J. Mater. Chem. A*, 2022, **10**, 7668–7676.
24 J. Huang, K. Wang and Z. Wei, *J. Mater. Chem.*, 2010, **20**, 1117–1121.
25 O.-N. Hur, S. Park, S. Park, B.-H. Kang, C.-S. Lee, J.-Y. Hong, S.-H. Park and J. Bae, *Mater. Chem. Phys.*, 2022, 285.
26 Q. Meng, K. Cai, Y. Chen and L. Chen, *Nano Energy*, 2017, **36**, 268–285.
27 D. Voiry, A. Goswami, R. Kappera, C. e Silva Cde, D. Kaplan, T. Fujita, M. Chen, T. Asefa and M. Chhowalla, *Nat. Chem.*, 2015, **7**, 45–49.
28 X. Zhu, Y. Guo, H. Cheng, J. Dai, X. An, J. Zhao, K. Tian, S. Wei, X. Cheng Zeng, C. Wu and Y. Xie, *Nat. Commun.*, 2016, **7**, 11210.
29 S. B. Artemkina, T. Y. Podlipskaya, A. I. Bulavchenko, A. I. Komonov, Y. V. Mironov and V. E. Fedorov, *Colloids Surf., A*, 2014, **461**, 30–39.
30 R. J. Smith, P. J. King, M. Lotya, C. Wirtz, U. Khan, S. De, A. O'Neill, G. S. Duesberg, J. C. Grunlan, G. Moriarty, J. Chen, J. Wang, A. I. Minett, V. Nicolosi and J. N. Coleman, *Adv. Mater.*, 2011, **23**, 3944–3948.
31 K. G. Zhou, M. Zhao, M. J. Chang, Q. Wang, X. Z. Wu, Y. Song and H. L. Zhang, *Small*, 2015, **11**, 694–701.
32 J. Li, P. Song, J. Zhao, K. Vaklinova, X. Zhao, Z. Li, Z. Qiu, Z. Wang, L. Lin, M. Zhao, T. S. Herng, Y. Zuo, W. Jonhson, W. Yu, X. Hai, P. Lyu, H. Xu, H. Yang, C. Chen, S. J. Pennycook, J. Ding, J. Teng, A. H. Castro Neto, K. S. Novoselov and J. Lu, *Nat. Mater.*, 2021, **20**, 181–187.
33 J. Zheng, H. Zhang, S. Dong, Y. Liu, C. T. Nai, H. S. Shin, H. Y. Jeong, B. Liu and K. P. Loh, *Nat. Commun.*, 2014, **5**, 2995.
34 M. Yamamoto, S. T. Wang, M. Ni, Y.-F. Lin, S.-L. Li, S. Aikawa, W.-B. Jian, K. Ueno, K. Wakabayashi and K. Tsukagoshi, *ACS Nano*, 2014, **8**, 3895–3903.
35 X. Zhang, Q. H. Tan, J. B. Wu, W. Shi and P. H. Tan, *Nanoscale*, 2016, **8**, 6435–6450.
36 J. Stejskal, I. Sapurina, M. Trchová, I. Šeděnková, J. Kovářová, J. Kopecká and J. Prokeš, *Chem. Pap.*, 2015, **69**, 1341–1349.
37 H. Hiura, T. W. Ebbesen, K. Tanigaki and H. Takahashi, *Chem. Phys. Lett.*, 1993, **202**, 509–512.
38 H. Kim and S.-H. Park, *Mater. Chem. Phys.*, 2022, 286.
39 A. Morozan, P. Jegou, S. Campidelli, S. Palacin and B. Jousselme, *Chem. Commun.*, 2012, **48**, 4627–4629.
40 H. M. N. Ahmad, S. Ghosh, G. Dutta, A. G. Maddaus, J. G. Tsavalas, S. Hollen and E. Song, *J. Phys. Chem. C*, 2019, **123**, 8671–8680.
41 C. Peng, H. Lyu, L. Wu, T. Xiong, F. Xiong, Z. Liu, Q. An and L. Mai, *ACS Appl. Mater. Interfaces*, 2018, **10**, 36988–36995.